Simulation of Bubble and Particle Interactions with Vortical Flows Using a Discrete Element Model

Justin Finn[*] and Sourabh V. Apte[*]

[*] School of Mechanical Industrial and Manufacturing Engineering, Oregon State University, Corvallis, OR 97333, USA

finnj@engr.orst.edu and sva@engr.orst.edu

Keywords: Euler-Lagrange, Bubbly Flows, Discrete Element Model, Two Way Coupling

Abstract

Discrete Element Model (DEM) is used to simulate bubble and particle interactions with vortical flows. In this Euler-Lagrange approach, volume-averaged Navier-Stokes equations are solved using a co-located grid finite volume method. The dispersed phase is assumed spherical and is modeled by tracking the centroids of the particles/bubbles in a Lagrangian frame. In addition to interphase momentum exchange, the volume occupied by the disperse phase is accounted for through fluid void fractions in the momentum and continuity equations. Interactions of the dispersed phase with vortical flows are investigated for both dilute and dense loadings. First, flow generated by the disperse phase motion are simulated to reproduce experimentally observed vortical flow features: (i) the breakup of a viscous blob of particles falling under the influence of gravity and (ii) the transient migration of a buoyant bubble plume. Finally, bubble entrainment and interaction with traveling vortex tube under dilute loadings are simulated in a two-dimensional approximation of the experiments by Sridhar and Katz (1999). It is shown that under some conditions, the entrainment of eight small bubbles, less than $1.1\,\mathrm{mm}$ in diameter, results in significant levels of vortex distortion, comparable to the experimental observations. We find that the bubble induced distortion is due almost entirely to volumetric displacement effects present in the DEM model. A relative reaction force, defined as the ratio of net bubble to fluid reaction to the local driving force of the vortex, is used to analyze the vortex decay rate. It is shown that the global increases in vortex decay rate are directly proportional to the magnitude of this highly local relative reaction.

Introduction

Bubbles, droplets, or particle laden turbulent flows are of interest in a broad array of important disciplines with applications to cavitation, sprays and spray combustion, coal combustion and fluidized beds. To date, our understanding of the phase coupling mechanisms which govern multiphase flow development is limited to low complexity problems in basic canonical geometries. Computational limits continue to restrict the use of complete, fully resolved direct numerical computations to engineering scale configurations for quite some time. It is therefore important to develop models capable of handling diverse flows containing large numbers of bubbles or particles that can accurately capture the interphase dynamics defining the characteristics of multiphase flows.

A recent review by van der Hoef et al. (2008) discusses present modeling strategies used for numerical simulation of gas/solid fluidized beds. The subset of methods currently capable of handling both large scale geometries and a large number of bubbles or particles can typically be classified as either Eulerian-Eulerian or Eulerian-Lagrangian. In an Eulerian-Eulerian or two-fluid model (for example, Ferrante and Elghobashi (2007)), both phases are treated as a continuum with unique fluid properties and two sets of conservation equations are solved. Because the idea of individual particles is not supported, closure models for interphase momentum transfer are required. In an Eulerian-Lagrangian simulation such as the ones presented in this paper, each element of the dispersed phase is treated as a sub-grid scale, spherical particle. Bubble or particle position is advanced in time in accordance with Newton's second law, with problem specific closures required for the various forces acting on the dispersed phase. Because the bubbles are assumed to be sub-grid in size their surface shape cannot be explicitly represented, and no interphase boundary condition is enforced.

Typical treatment of the dispersed phase as 'point particles' allows the bubbles to transfer momentum as point sources but does not account for the volume of fluid which they displace. To further advance these models, the effects of fluid volume displaced by the dispersed phase, termed in this work as *volumetric coupling*, is considered using a variable density form of

the governing equations, as in Prosperetti and Zhang (1995), Joseph et al. (1990), van der Hoef et al. (2008). Specifically, the importance of volumetric coupling for dilute as well as dense loading of the disperse phase is evaluated.

Test cases dealing with dispersed phase interactions with single, distinct vortical structures can be good building blocks for understanding more complex problems, and have been studied by several groups. Sridhar and Katz (1995) and Van Nierop et al. (2007) used experimental techniques to develop models for bubble motion in non-uniform flow, with particular emphasis placed on the determination of the bubble lift coefficient. Oweis et al. (2005) used fully resolved, front tracking methods to solve the flow field around deforming and cavitating bubbles during entrainment by a stationary Gaussian vortex. They compared bubble capture time predicted by a passive point particle method with the front tracking results as well as experimental data under similar conditions. They found their point particle method was able to accurately capture the trajectory of bubble entrainment, up to the point of bubble cavitation and volume growth in the vortex core. Sridhar and Katz (1999) observed the effects that bubbles, with diameter $400\mu m < d_b < 1,100\mu m$, had on the structure of piston generated vortex rings. Their experimental results show that for a small number of entrained bubbles, at low overall volume fraction, significant distortion of the ring structure was possible under certain conditions. In significantly distorted vortices, the presence of the bubbles resulted in a fragmented core, with multiple regions of higher vorticity. They supplied good analytic rationalization of their results, including the bubble settling locations, and the observed vortex distortion at low bubble volume fraction.

In more general turbulent flows, bubbles and particles are known to accumulate in certain regions. Bubbles are attracted to the vortex cores, while particles will collect in the the high shear, low vorticity regions. This preferential accumulation has been studied by Ferrante and Elghobashi (2003); Climent et al. (2007); Mazzitelli et al. (2002) and can be responsible for significant flow modulation. More complex engineering scale problems have also been simulated with the Eulerian-Lagrangian approach. There are growing bodies of literature dedicated to bubble column reactors (Darmana et al. (2005); Hu and Celik (2008)) and combustion chambers (Apte et al. (2003); Moin and Apte (2006)) which show promising results for the technique.

In this work it is shown that volumetric displacement effects can be of importance even under dilute loadings, especially for bubbly flows by simulating interactions of small number of small bubbles with traveling vortex tube. First, the numerical model and its implementation

is verified by simulating interactions of disperse phase with vortical structures under dense loadings. The problems vary in their level of complexity, but each demonstrate the ability of the present methods to capture bubble or particle induced flow phenomenon with subgrid modeling of the disperse phase. In the next section, the governing equations and mathematical formulation are outlined. Various verification test cases, chosen to show the accuracy of the methods and the importance of volumetric coupling, are discussed next. Finally, bubble interactions with a traveling vortex tube are studied in detail for dilute loadings. A correlation is developed for the bubble induced vortex decay rate, based on the relative magnitude of the net bubble to fluid reaction.

Mathematical Formulation

In Discrete Element Method (DEM), the motion of the fluid phase is computed using Direct Numerical Simulation (DNS) or large-eddy simulation (LES), and Lagrangian particle tracking is used to solve the motion of spherical subgrid scale dispersed phase. Dispersed phase motion is calculated from Newton's second law, with models for gravity, pressure, lift, drag, and added mass forces. A bubble to fluid reaction is calculated to account for two-way momentum exchange. In addition, the present formulation is derived from volume averaging, and accounts for *volumetric* displacement of the fluid by the dispersed phase. In this section, we use subscripts b to denote the dispersed phase and f for the continuum phase. We refer to individual dispersed phase element as a 'bubble'. However, the formulation is equally applicable to gas/solid particle systems.

Dispersed Phase Motion In the Lagrangian reference frame, the equations of motion may be written for each bubble as a system of ordinary differential equations:

$$\frac{d}{dt}(\mathbf{x}_b) = \mathbf{u}_b \qquad (1)$$

$$m_b\frac{d}{dt}(\mathbf{u}_b) = \sum \mathbf{F}_b \qquad (2)$$

where $\mathbf{F}_b$ is the net force acting on each bubble and has the following contributions:

$$\sum \mathbf{F}_b = \mathbf{F}_G + \mathbf{F}_P + \mathbf{F}_{AM} + \mathbf{F}_D + \mathbf{F}_L \qquad (3)$$

The gravitational force, $\mathbf{F}_G$, is the weight of the bubble.

$$\mathbf{F}_G = \rho_b V_b \mathbf{g} \qquad (4)$$

where V_b is the bubble volume and $\mathbf{g}$ is the gravitational acceleration. The pressure force, $\mathbf{F}_P$, is the force on the

bubble due to the total pressure gradient, including the hydrostatic contribution.

$$\mathbf{F}_P = -V_b \nabla P \qquad (5)$$

The added mass force, $\mathbf{F}_{AM}$, is the force which would be exerted on the volume of fluid displaced by the presence of the bubble. It is given by

$$\mathbf{F}_{AM} = \rho_f V_b C_{AM} \left(\frac{D\mathbf{u}_{f,b}}{Dt} - \frac{D\mathbf{u}_b}{Dt} \right), \qquad (6)$$

where $\mathbf{u}_{f,b}$ represents the fluid velocity interpolated to the bubble centroid location. For small, spherical bubbles and particles, it is generally accepted that $C_{AM} = 0.5$. Inter-bubble collision forces are neglected in this work. The bubble drag force, $\mathbf{F}_D$ arises due to a difference in bubble and fluid velocities. It is given by:

$$\mathbf{F}_D = -\frac{1}{2} C_D \rho_f \frac{\pi d_b^2}{4} |\mathbf{u}_b - \mathbf{u}_{f,b}|(\mathbf{u}_b - \mathbf{u}_f) \qquad (7)$$

where $A_b = \frac{\pi}{4} d_b^2$ is the frontal area of the bubble. The bubble slip velocity, $(\mathbf{u}_b - \mathbf{u}_{f,b})$ is evaluated using the local velocity field near the bubble of interest. The lift force, F_L, arises for bubbles in shear or rotating flow and has been the subject of much discussion in the literature. In general, it can be expressed as:

$$\mathbf{F}_L = -C_L \rho_f V_b (\mathbf{u}_b - \mathbf{u}_{f,b}) \times (\nabla \times \mathbf{u}_{f,b}) \qquad (8)$$

Where C_L is the lift coefficient. At Reynolds numbers much greater than one, C_L and C_D are know by empirical relations only, and we choose expressions for these values on a case by case basis. All cases except the bubble column use the standard drag curve of Schiller and Naumann (1935) for solid sphere drag

$$C_D = \frac{24}{Re_b}(1 + 0.15 Re_b^{0.687}) \qquad (9)$$

The bubble column case uses expressions suggested by Darmana et al. (2006)

$$
\begin{aligned}
C_L^{bc} &= 0.5, \qquad C_D^{bc} = \max\left[C_D^{Re},\ C_D^{Eo} \right] \\
C_D^{Re} &= \min\left[\frac{16}{Re_b}(1 + 0.15 Re_b^{0.687}), \frac{48}{Re_b} \right] \\
C_D^{Eo} &= \frac{Eo}{Eo + 4}, \qquad Eo = \frac{(\rho_f - \rho_b) g d_b^2}{\sigma}
\end{aligned}
\qquad (10)
$$

The Gaussian vortex case, and the traveling vortex tube case use the strong lift coefficient suggested by Sridhar and Katz (1995).

$$C_L^{vx} = 0.22\alpha^{-3/4}; \qquad \alpha = \frac{|\nabla \times \mathbf{u}_{f,b}| d_b}{2|\mathbf{u}_{f,b} - \mathbf{u}_b|} \qquad (11)$$

The falling blob case uses the lift coefficient suggested by Saffman

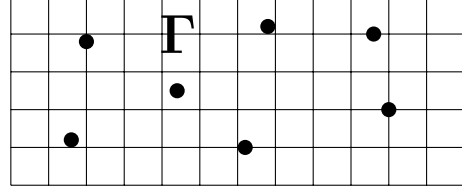$$C_L^{blob} = \frac{1.61 \frac{6.0}{\pi}}{d_b} \sqrt{\mu_f / (\rho_f \omega)} \qquad (12)$$

Figure 1: Illustration of the fluid domain, Γ containing a subgrid scale dispersed phase.

Variable Density Fluid Formulation Consider a domain Γ which contains a continuous fluid phase, and a dispersed bubbly or particulate phase as shown in figure 1. Each element of the dispersed phase has a finite, characteristic diameter, d_b, and occupies a volume V_b. The finite size of the disperse phase may be accounted for by introducing the fluid and disperse phase volume fractions, Θ_f and Θ_b, where $\Theta_f = 1 - \Theta_b$. In doing so, the volume averaged continuity equation becomes (Joseph et al. (1990); Zhang and Prosperetti (1997); Jackson (1997))

$$\frac{\partial}{\partial t}(\rho_f \Theta_f) + \nabla \cdot (\rho_f \Theta_f \mathbf{u}) = 0 \qquad (13)$$

Note that in this form, the fluid velocity field is not *divergence free*, even for an incompressible fluid (Apte et al. (2007)). Similarly, the fluid momentum equation becomes (using the model formulation suggested by Gidaspow (1994),

$$
\begin{aligned}
\frac{\partial}{\partial t}(\rho_f \Theta_f \mathbf{u}) &+ \nabla \cdot (\rho_f \Theta_f \mathbf{u}\mathbf{u}) = -\nabla P + \\
&\nabla \cdot (\Theta_f \mu_f (\nabla \mathbf{u} + \nabla \mathbf{u}^T)) + \Theta_f \rho_f \mathbf{g} + \mathbf{f}
\end{aligned}
\qquad (14)
$$

The force $\mathbf{f}$ is not present in a single phase flow, and arises due to interphase momentum transfer from the bubbles.

$$\mathbf{f} = -\left(\mathbf{F}_P + \mathbf{F}_D + \mathbf{F}_L + \mathbf{F}_{AM} \right). \qquad (15)$$

The interphase reaction force ($\mathbf{f}$) can be split into (i) the contribution from the pressure force and (ii) a net drag from all other forces as described by van der Hoef et al. (2008). The pressure force then results in the force density $+\Theta_b \nabla P$. This reaction term related to the pressure gradient can be combined with the pressure gradient in the momentum equation to obtain:

$$
\begin{aligned}
\frac{\partial}{\partial t}(\rho_f \Theta_f \mathbf{u}) &+ \nabla \cdot (\rho_f \Theta_f \mathbf{u}\mathbf{u}) = -\nabla P - \Theta_f \rho_f \mathbf{g} \\
&\nabla \cdot \left(\Theta_f \mu_f (\nabla \mathbf{u} + \nabla \mathbf{u}^T) \right) + \mathbf{f}' + \underbrace{\Theta_b \nabla P}_{\mathbf{F}_P \text{ Force Density}},
\end{aligned}
\qquad (16)
$$

where $\Theta_b \nabla p$ is the Eulerian force density obtained from the pressure force and $\mathbf{f}'$ is the Eulerian force density constructed from the Lagrangian force on the bubbles without the pressure force (equation 15 without the

pressure force, $\mathbf{F}_P$). Noting that $\Theta_b + \Theta_f = 1$, the above equation can be re-written in a more commonly used form by combining the first and last terms on the right-hand side of the above equation (Gidaspow (1994); van der Hoef et al. (2008)),

$$\frac{\partial}{\partial t}(\rho_f \Theta_f \mathbf{u}) + \nabla \cdot (\rho_f \Theta_f \mathbf{uu}) = -\Theta_f \nabla (P) +$$
$$\nabla \cdot \left(\Theta_f \mu_f (\nabla \mathbf{u} + \nabla \mathbf{u}^T)\right) - \Theta_f \rho_f \mathbf{g} + \mathbf{f}', \quad (17)$$

where $\mathbf{f}'$ contains summation of all reaction forces in equation 15 except the pressure force. This formulation is commonly used in gas-fluidized beds (Gidaspow (1994); van der Hoef et al. (2008)). In case of Reynolds averaged Navier-Stokes equations or large-eddy simulations, the above equations should be time-averaged or spatially filtered using density-weighted Favre averaging. Using the form in equation 17; however, gives rise to an additional unclosed term $-\overline{\Theta_f \nabla P}$. It is therefore advantageous to use the original form (equation 14), resulting in standard variable density LES equations Moin and Apte (2006). In this case, the reaction due to the pressure force is treated *explicitly*.

We choose to use the form of equation 14 for numerical implementation. The formulation for the fluid phase given by equations 13, 14, and 15 represents what we will refer to as *volumetric coupling*, where both bubble size and momentum transfer are accounted. The numerical solution of the fluid and bubble motion proceeds in the framework of a parallel, fractional step, finite volume solver (Shams (2010)).

Bubble entrainment in a Gaussian vortex

To verify the accuracy of the solver, the entrainment of a single bubble into a stationary Gaussian vortex is considered. A schematic of the problem is shown in figure 2a. A buoyant bubble is released in the vicinity of the vortex with core radius, r_c. The Gaussian vortex is a planar vortex with initial circulation Γ_0 whose vorticity distribution is a Gaussian function of radius. There is no radial velocity component, and the the tangential velocity can be expressed as

$$u_\theta(r) = \frac{\Gamma_0}{2\pi r}\left(1 - e^{-\eta_1(r/r_c)^2}\right). \quad (18)$$

The vorticity and maximum tangential velocity are

$$\omega(r) = \frac{\Gamma_0 \eta_1}{\pi r_c^2} e^{-\eta_1(r/r_c)^2}; \quad u_c = \eta_2 \frac{\Gamma_0}{2\pi r_c}, \quad (19)$$

where η_1 and η_2 are constants. Assuming axial symmetry, the hydrodynamic pressure gradient is $\partial p/\partial r = \rho u_\theta^2/r$. This flow has been used previously by Oweis et al. (2005), as a model for wingtip vortices in their study of bubble capture and cavitation inception. Under

the right conditions, ie. the vortex is strong enough, the bubble will become entrained in the vortex core. During this process, it may circle the core several times before eventually reaching a settling location with relative coordinates r_s, θ_s measured from the vortex center.

A total of 14 individual cases of single bubble entrainment are simulated using the passive, one-way coupling approach. Variables relevant for the setup of the parametric study are summarized in table 1. The domain size is $7r_c \times 7r_c \times 0.4\ r_c$. The no-slip condition is imposed at boundaries in the X and Y directions, and the domain is periodic in the Z direction. Uniform grid spacing is used throughout the domain with $\Delta = 1.25mm$ and total number of grid points as $64 \times 64 \times 4$ in the X, Y and Z directions. The flow solver time step is $\Delta t = 0.4ms$ whereas the bubbles advanced with a time-step of $2\ \mu s$ using subcycling per time-step. The velocity field of equation 18 is applied as an initial condition everywhere in the domain, creating a clockwise vortex. A single bubble is released during the first timestep at $r = r_c$, $\theta = 0$. In all cases, gravitational acceleration is $\mathbf{g} = -9.81m/s^2$ in the Y direction, and typical properties of water and air are assumed. For the parameters shown in table 1, the bubble Stokes numbers ($St_b = \bar{\omega} d_b^2/36\nu$, where $\bar{\omega} = \Gamma_0/\pi r_c^2$) are between 0.5 and 5.7.

Force balance in vortical flow At the settling location, there is no motion of the bubble relative to the vortex, meaning that all forces acting on the bubble are in balance. This is illustrated in figure 2b, where we have included the lift, drag, pressure, added mass, and gravity forces. Note that the pressure force has been split into its dynamic and hydrostatic contributions. For the clockwise vortex shown, the settling location will be in first quadrant of the core where the fluid velocity is turning downward. Mazzitelli et al. (2002) showed that it is primarily the lift force, which acts perpendicular to the vorticity and slip velocity vectors, that is responsible for bubble accumulation in the downward velocity side of vortices such as this one. If the flow is steady and axisymmetric then the directionality of the other forces in figure 2b can also be deduced. The net buoyancy force which acts upward is due the addition of the hydrostatic pressure force, $\mathbf{F}_{PH}$ and the bubble weight, $\mathbf{F}_G$. The added-mass and dynamic pressure forces act in the direction of negative dynamic pressure gradient. Neglecting outside disturbances, this will be toward the vortex center. The drag force acts in the direction of the slip velocity vector which, for a stationary bubble in an axisymmetric vortex, is perpendicular to the settling location vector, $\mathbf{r}_s$.

Since the velocity, vorticity, and pressure gradient are known functions of radius in the Gaussian vortex, it is

Table 1: Computational parameters used for the Gaussian vortex.

r_c[mm]	η_1	η_2	Δ[mm]	N_{grid}	$\Gamma_0[m^2/s]$	$d_b[\mu m]$
11.45	1.27	0.715	1.25	64x64x4	0.02, 0.03, 0.04, 0.05	500, 700, 900, 1,100, 1,300
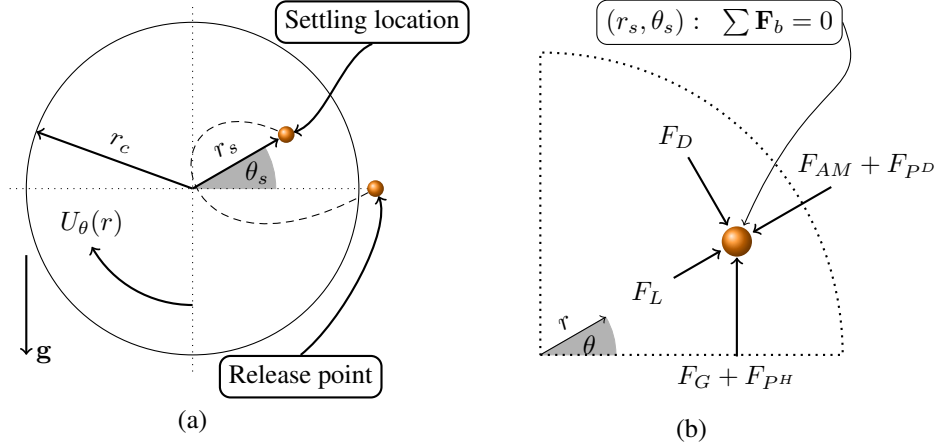
Figure 2: Schematic of a bubble entrained in a vortex and the forces which influence its settling location, (r_s, θ_s).

possible to obtain analytic expressions for the settling coordinates (r_s, θ_s) of entrained bubbles using force balances in the radial and azimuthal directions. Van Nierop et al. (2007) performed such an analysis to develop uncoupled expressions for bubble settling coordinates in *forced*, rotating flow. Here, we employ a similar approach to obtain coupled expressions for settling location in the *free*, Gaussian vortex. Using figure 2b as a guide, a force balance in the azimuthal direction reveals that the drag force is balanced entirely by a component of the net buoyancy force.

$$(\mathbf{F}_G + \mathbf{F}_{PH})\cos(\theta_s) = \mathbf{F}_D \qquad (20)$$

In the radial direction, there is a more ambiguous balance between the lift force, the dynamic pressure force, the added mass force and a component of the gravity force.

$$\mathbf{F}_B \sin\theta_s + \mathbf{F}_L = \mathbf{F}_{PD} + \mathbf{F}_{AM} \qquad (21)$$

The dynamic pressure force and added mass force can be combined,

$$\mathbf{F}_{PD} + \mathbf{F}_{AM} = (1 + C_{AM})\rho_f \frac{u_\theta^2}{r_s} \qquad (22)$$

Inserting this and the expressions for $\mathbf{F}_D$, $\mathbf{F}_L$ and $\mathbf{F}_G$ into equations 20 and 21, the force balances can be rearranged into two coupled equations for r_s and θ_s:

$$\cos(\theta_s) = \frac{3C_D U_\theta^2}{4d_b \mathbf{g}\left[\frac{\rho_b}{\rho_f} - 1\right]} \qquad (23)$$

$$r_s = \frac{(1 + C_{AM})U_\theta^2}{\left[\frac{\rho_b}{\rho_f} - 1\right]\mathbf{g}\sin(\theta_s) + C_L U_\theta \omega} \qquad (24)$$

If the flow field inside the vortex core is known (Gaussian, Taylor-Green, Rankine, etc.), and the drag and lift coefficients are specified functions of U_θ and ω, then equations 23 and 24 can be solved iteratively for the bubble settling coordinates. Figure 3 shows a comparison of the settling location predicted by the DEM model with passive, one way coupling, to the values predicted from solving equations 23 and 24 for the 14 individual cases, showing good agreement. In the analytic prediction, the value of Γ_0 has been decreased by 12% in all calculations to compensate for the viscous decay which happens before the bubble comes to rest. Time averages of the numerical, 1-way settling location are taken over a period of 0.1 seconds, 1.8 seconds after injection.

LES of a Rising Bubble Column

For this test case, the geometry selected corresponds to the 'Becker case' (Becker et al. (1994)), which has become an almost standard case in the chemical engineering literature for dense bubbly flows. The domain is shown in figure 4(a). Characteristic dimensions and relevant simulation parameters are summarized in table 2.
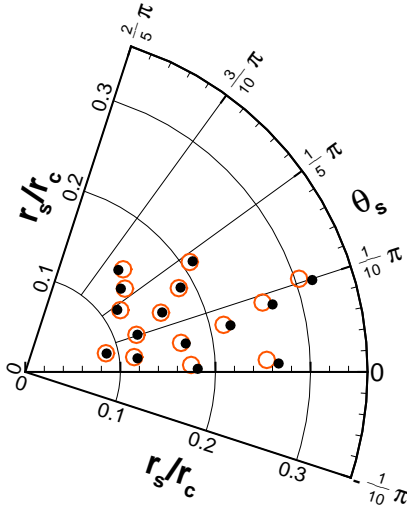
Figure 3: Settling location of bubbles in the core of the stationary Gaussian vortex: (●) analytical, (○) DEM.

(a) Geometry   (b) Avg. Velocity field

Figure 4: (a)Bubble column geometry showing the instantaneous bubble locations. Points A and B correspond to the location of two velocity probes. (b) Contours of time averaged Y component of fluid velocity. Streamtraces show the time averaged velocity field.

All boundaries are assigned a no-slip condition except for the top wall at $Y = 1.5$, where a slip condition ($u_y = 0$) is applied to approximate the experimental free surface. Air bubbles are continuously injected into the water filled domain from a disk located on the bottom wall with a flow rate of $1.6\ l/min$ and a superficial gas velocity of $0.66m/s$. The injection disk is $0.04m$ in diameter and located $0.15m$ from the left hand wall. At this gas flow rate, the fluid and bubble motion is known experimentally to be periodic in nature. We use this test case to see if the present methods can capture the transient behavior. A Dynamic Smagorinsky model for variable density fluid flow is used to compute the subgrid scale fluid stress.

Table 2: Parameters for the bubble column case.

L_x, L_x, L_x	0.5m, 1.5m, 0.08m
n_x, n_y, n_z	80, 150, 15
Gas Flow Rate	$1.6\ l/min$
Superficial gas velocity	$0.66mm/s$
Injection location	$(x, y, z) = (0.15, 0, 0)$
Injection Diameter	$d_{inj} = 0.04m$
Bubble Diameter	$1.6mm$
Bubble Density	$1.2kg/m^3$
Liquid Density	$1,000kg/m^3$
Liquid Viscosity	$10^{-3}Ns/m^2$
Probe 'A' (x, y, z)	0.035m, 0.9m, 0.04m
Probe 'B' (x, y, z)	0.45m, 1.05m, 0.04m

Figure 4(b) shows the streamlines corresponding to the average velocity field in the X-Y midplane. In the lower half of the domain, a large clockwise vortex is generated by the bubbles rising along the left hand wa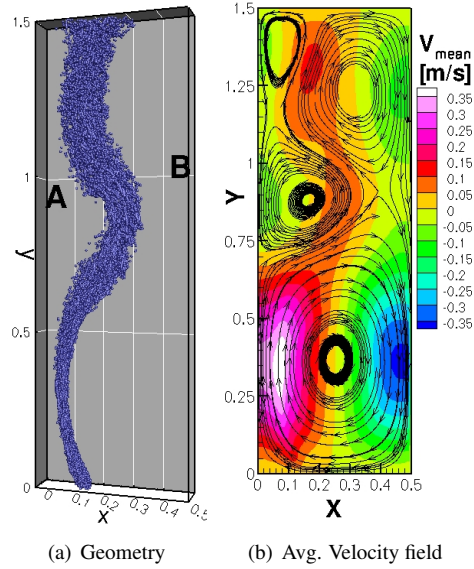ll. The upper half is highly transient, and marked by the periodic migration of the bubble plume in the X direction. This migration corresponds with the growth and collapse of several secondary vortices in the upper regions of the domain. The periodicity of the bubble plume is shown in figure 5 where we have plotted 8 snapshots of instantaneous bubble positions, each 7 seconds apart. In figure 5a, the plume is firmly directed against the left wall through most of its length due to the strong lower vortex. A secondary, counter-clockwise vortex located in the upper left corner of the domain pushes the top of the plume to the right. In figures 5b through 5e, this secondary vortex strengthens and slides downward along the left hand wall, creating a bulge in the plume. This bulge cannot travel into the lower part of the plume due to the size and strength of the main circulation region, and eventually it collapses, as a new counter-clockwise vortex is created in the upper left corner (see figures 5f through 5h).

The periodic nature of the liquid phase is shown in figure 6, where we plot the vertical velocity in time for points 'A' and 'B' as shown in figure 4(a). The magnitude of the velocity peaks at these two points is similar to the values measured in the experiments of Sokolichin and Eigenberger (1999). We observe an average oscillation period of about 49 seconds, which is 8 seconds longer than observed in the experiments. Deen et al. (2000) and Delnoij et al. (1997) also had trouble matching the oscillation period in their computations. There
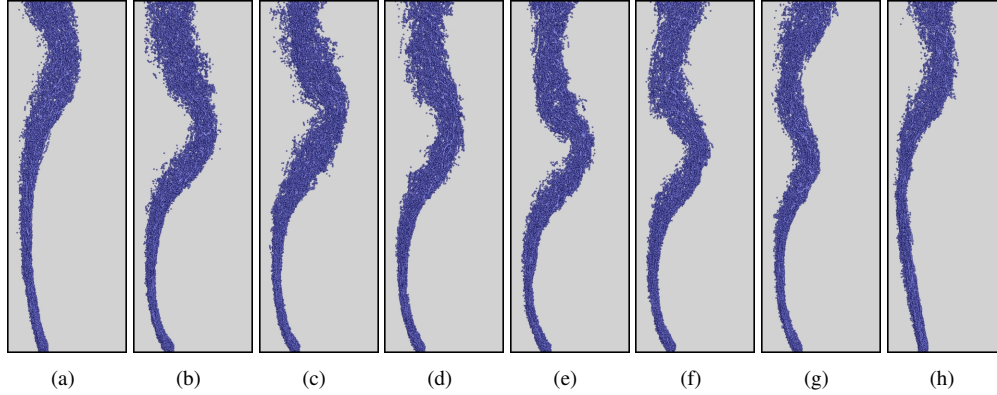
Figure 5: Periodic migration of the bubble swarm. Each figure is a snapshot of instantaneous bubble positions, with 7 seconds between each frame. The first (a) and last (h) frame are chosen to correspond with the approximate beginning and end of one cycle.

are numerous factors which play a role in the oscillation period including grid resolution, bubble size, lift coefficient and drag coefficient. Also it was found that small changes in the injection velocity and inlet conditions can influence the oscillation periods. The LES results with volumetric coupling, however, do show the experimentally observed trends of periodic jet oscillation and large scale vortical regions.
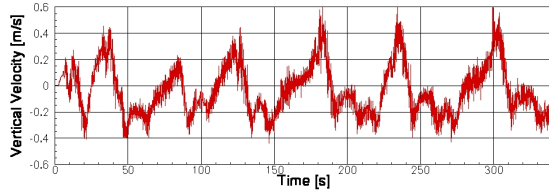
(a) Point 'A' vertical velocity
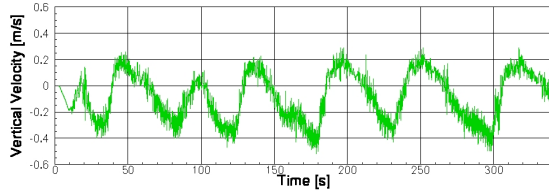
(b) Point 'B' vertical velocity

Figure 6: Fluid velocity at the points 'A' and 'B' shown in Figure 4a.

Three-Dimensional Falling 'Blob'

This test case is included to show the applicability of methods to a flow driven entirely by particle motion. Consider a three dimensional sphere composed of several thousand tightly packed rigid particles. The fluid region containing this particle 'blob' has a uniform ini-

tial particle volume fraction, Θ_{p0}. Both the local density, ρ_f, and viscosity, μ_f, vary according to this volume fraction. In the high particle number, N_p, limit, the behavior of this particle/fluid system is analogous to a viscous, droplet dissolving in a fluid with which it is miscible. For two such fluids, the surface tension force at the droplet interface vanishes, and the droplet dynamics are governed by viscous and inertial forces. The problem may be described in terms of the density ratio, viscosity ratio, blob Reynolds number, and blob Froude number:

$$
\begin{aligned}
DR &= \rho_b/\rho_f; \;\; R = \mu_b/\mu_f \\
Re_b &= \frac{\rho_f U D_b}{\mu_f}; \;\; Fr_b = \frac{U}{\sqrt{gD_b}}
\end{aligned}
$$

Mitts et al. (1996) used the miscible fluid analogy to study the dynamics of deformation and breakup of droplets in the supercritical regime. Supercritical conditions are present in many rocket engines, where high temperatures and pressures are required, and many questions remain about the behavior of the fuel-air mixture. They were able to classify the miscible droplet behavior into several sub-regimes based on the viscosity ratio and droplet Reynolds number for density ratios near unity. In a computational study, Walther and Koumoutsakos (2001)(W&K) used adaptive vortex methods and Lagrangian particle tracking to model several of these sub-regimes, including the multi-mode bag vortex ring sub-regime, which will be the focus of this validation case. In their work, they characterized the speed of a falling blob of particles using the Hadamard and Rybczyński (H-R) formula for the speed of a viscous, spherical drop descending under the force of gravity :

$$
U = U_{HR} = \frac{(\rho_d - \rho)gD_b^2}{12\mu} \frac{\mu + \mu_d}{\mu + \frac{3}{2}\mu_d} \tag{25}
$$

In this test case, $97,233$ solid particles are arranged into a spherical shape in an initially quiescent fluid. The particles are heavier than the liquid, and fall under the influence of gravity. The local viscosity of the fluid is varied at the grid faces:

$$\mu = \mu_f + \Theta_p(\mu_p - \mu_f) \tag{26}$$

where Θ_p is the particle volume fraction of the associated control volumes. The initial volume fraction is obtained from the following expression derived by Lundgren (1972) for high volume fractions:

$$\frac{\mu_p}{\mu_f} \approx \frac{1}{1 - \frac{5}{2}\Theta_{p0}} \tag{27}$$

The computational parameters were selected so that comparisons could be made with both experimental and numerical studies of the bag vortex ring sub-regime. The characteristic velocity, U, is defined using the H-R formula (equation 25). In doing so, the problem can be specified completely by assigning the density ratio, viscosity ratio, Reynolds number, and Froude number. For clarity, all parameters used in the setup of this case are summarized in table 3. Note that the particle density is greater than the blob density due to the initial volume fraction which is less than unity.

Table 3: Parameters used for the setup of the three dimensional falling 'blob.'

Parameter	Value
D_b	100 mm
d_p	1.572 mm
N_p	97,233
g	9.81 m/s^2
Θ_{p0}	0.388
μ_b/μ_f	35.0
μ_f	0.001 pa-s
ρ_b/ρ_f	1.6
ρ_f	1.0 kg/m^3
ρ_p	2.544 kg/m^3
Re_b	330
Fr_b	3.332
Domain Size	$10D_b$ x $10D_b$ x $10D_b$
Grid Size	64 x 64 x 64

Three different DEM models are considered and are summarized in table 4. Model 1 is intended to be similar to the one used by W&K. Here, the particle motion is affected only by gravity, and drag forces, and the particle to fluid momentum coupling is a result of the drag force only. The fluid density is constant everywhere. In model 2, the added mass force, lift force, and pressure force are also considered in the particle equation of motion,

and the momentum coupling to the fluid includes these additional terms. In model 3, the variable density, volumetric coupling model is used, and the fluid density, ρ_f, varies according to the local particle volume fraction.

Table 4: Comparison of the 3 present DEM models and the model used by Walther & Koumoutsakos in the falling blob case

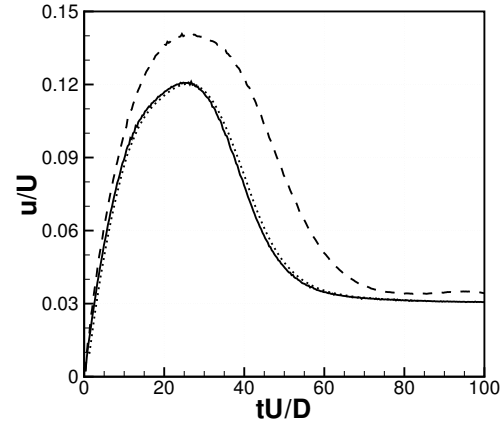| Model	F_G	F_D	F_L	F_{AM}	F_P	Variable Density
W&K	Yes	Yes	No	No	No	No
#1	Yes	Yes	No	No	No	No
#2	Yes	Yes	Yes	Yes	Yes	No
#3	Yes	Yes	Yes	Yes	Yes	Yes

Figure 7: Blob speed non-dimensionalized by the H-R velocity as a function of non dimensional time (——)Model 1, ($\cdots$)Model 2, (- - -)Model 3.

The speed of the center of gravity of the descending blob is shown in figure 7. In the present case, the peak blob Reynolds number based on blob velocity and initial diameter is 40 for models 1 & 2 and 46 for model 3. For the present viscosity ratio of 35, this puts the results within the bag vortex sub-regime observed by Mitts et al. and simulated by W&K. The blob speed over the time simulated is nearly the same for models 1 and 2, showing that the net effect of lift, added mass and pressure forces is negligible for this case. Further, this shows that the increase in blob velocity shown by model 3 is due entirely to the volumetric effects. The blob accelerates to a peak non-dimensional velocity of $0.12U_{HR}$ for models 1 & 2 and $0.14U_{HR}$ for model 3 at a non-dimensional time of about 27. The difference in speeds of the falling blob suggests that the model for drag force used in the volumetric coupling needs modifications to
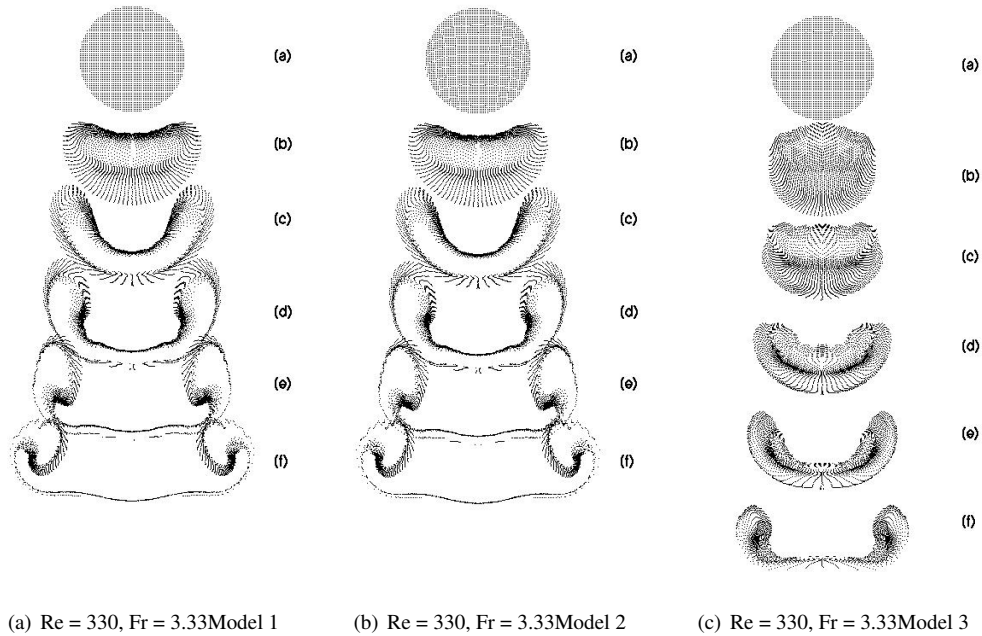
(a) Re = 330, Fr = 3.33 Model 1　　(b) Re = 330, Fr = 3.33 Model 2　　(c) Re = 330, Fr = 3.33 Model 3

Figure 8: Cross section of falling blobs with $\rho_b/\rho = 1.6$ and $\mu_b/\mu = 35$ at different non dimensional times (tU/D) = (a) 0.00, (b)7.18, (c) 10.77, (d) 14.36, (e) 17.94, (f) 21.53. [Left] Vortex method simulation of Walther and Koumoutsakos (2001) at Re = 180 & Fr = 1.79. [Center & Right] Present results of model 1,2,& 3 at Re = 330, Fr = 3.33.

account for local changes in the fluid volume fractions.

Figure 8 compares cross sections of the blob at different non-dimensional times throughout this period of initial acceleration for each model. During this time, the blob deforms into a spherical cap shape as the particles in the center of the blob descend faster then the ones on the edge. This is due to viscous action at the edge of the blob which causes the roll-up of a vortex ring around the blob. The ring travels with the blob and causes continued spreading in plane normal to the falling direction. Qualitatively similar spreading was observed by Walther and Koumoutsakos (2001) with their vortex method predictions.

The differences in blob shape during the acceleration to peak velocity can be explained by the variable density effects of model 3. With volumetric coupling considered, the fluid density in the blob region is lowered in proportion to the particle volume fraction. This results in a lower resistance to particle motion and helps to accelerate the fluid *with* the blob. The blob deforms to a spherical cap shape rapidly in models 1 & 2 because the particles on the bottom of the blob do the work of pushing the initially quiescent fluid out of the way, while the particles on the top accelerate. In model 3, this effect is delayed by the lowered fluid resistance in areas of high volume fraction, meaning the blob accelerates in a more uniform fashion. At later times, the blob spreads and forms a bag vortex ring which travels with the blob.Once

the ring is spread sufficiently wide ($tU/D > 60$), the net volumetric effects are decreased, and the blob velocity for model 3 approaches that of models 1 & 2.

The three dimensional shape of the blob is shown at different stages of breakup examined by Mitts et al. (1996) in figure 9. After the peak velocity is reached, the blob continues to expand into an unstable ring like shape. The particles collect in the high-shear regions on the downward velocity side of the vortex ring, and drive the circulation of the ring (figure 9(b)). At still later times, the ring becomes unstable, and the particles cluster into four regions of high volume fraction(figure 9(c)). These clusters accelerate as the original blob did, and form four new vortex rings. The initial deformation, the bag vortex ring roll up and instability, and subsequent droplet splitting are all predicted and show good levels of similarity with the experimental observations.

Bubble in a Traveling Vortex Tube

Interactions of micro-bubbles with a traveling vortex corresponding to the experiments by Sridhar and Katz (1995, 1999) are investigated. Specifically, they observed that with dilute loading of eight small bubbles, once entrained into a vortex ring, could deform the ring significantly. The simulations are setup to investigate if the DEM approach with volumetric effects can capture this phenomenon.

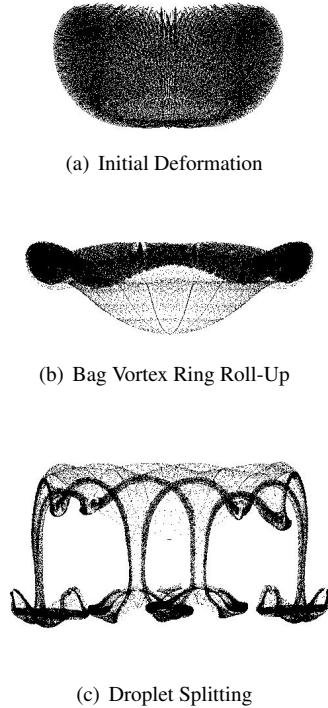The computational domain and the evolution of an

(a) Initial Deformation

(b) Bag Vortex Ring Roll-Up

(c) Droplet Splitting

Figure 9: Comparison of the present results of model 3 with the experimental results of Mitts et al. (1996) for the bag vortex ring sub-regime of the multi-mode breakup category.
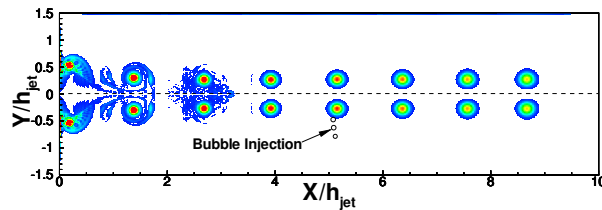

Figure 10: Computational domain and vortex tube evolution: (a) Two, symmetric vortex tubes are created by an inlet jet pulsed at $X = 0$. Contours show vorticity out of the plane as the undisturbed vortex travels downstream. Location of bubble injection is $X/h_{jet} = 5.0$

undisturbed pair of vortex tubes are shown in Figure 10. There is an inflow boundary at the left wall, an outflow condition at the right boundary, and walls on the top and bottom. The total domain size is $X/h_{jet} = 10$, $Y/h_{jet} = 3$ and is centered at $Y/h_{jet} = 0$. At the left inlet boundary, a jet is pulsed for 0.27 seconds into the initially quiescent domain, which causes the roll up of two symmetric vortex tubes. The contours in figure 10 show the diffusion of high vorticity as the vortex tube travels downstream. Table 5 lists the computational parameters used in this study. The inflow velocity is a function of time, and is described by a sixth-order polynomial to match the experimental conditions. To keep the size of the computation small and allow several parametric studies, a two-dimensional domain is simulated with periodic conditions in the spanwise direction giving rise to a vortex-tube. A uniform Cartesian grid is used throughout the area below the line of symmetry with a total of 800×121 elements in the X and Y directions.

Table 5: Parameters for the traveling vortex tube case.

Parameter	Value
ρ_f, ν_f	$1,000\ kg/m^3$; $10^{-6}\ m/s^2$
Domain Size	1m × 0.15m × 0.005m;
Grid Size	$800 \times 121 \times 4$
Jet height (h_{jet})	0.1 m
Inflow Time	0.27 s
Vortex Strength, $\Gamma_0 (m^2/s)$	0.0159, 0.0207, 0.0254
Bubble Size (μm)	500, 700, 900, 1,100
Inflow Velocity	$U(t) = \sum_{n=0}^{6} a_n t^n$
a_6, a_5, a_4, a_3	62278; -47082; 13686; -2062
a_2, a_1, a_0	159.5; -1.289; 0.006

At a value of $X/h_{jet} = 5.0$, eight bubbles are injected below and in front of the vortex core. Due to buoyancy, the bubbles rise around the rear of the vortex and are swept into the downward velocity region on the forward side of the passing core. A parametric study is performed to determine how bubble settling location and vortex structure are affected by bubble size and vortex strength. Depending on the Stokes number, the bubbles may circle the core multiple times before ultimately reaching their final settling location, where their average motion relative to the vortex center is zero. Once they have reached this state, the settling coordinates (r_s, θ_s) are averaged over all bubbles and in space over a distance of $5.2 X/h_{jet} < X_{vx} < 5.8 X/h_{jet}$. The average settling radius for each case is plotted against the non-dimensional parameter $\mathbf{g} d_b^3 / 8 \Gamma_0^2$ (ratio of buoyancy force to hydrodynamic pressure gradient) in figure 11 alongside the experimental data. Even at this small overall volume fraction, the local volume displacement effects are crucial in obtaining the correct bubble settling

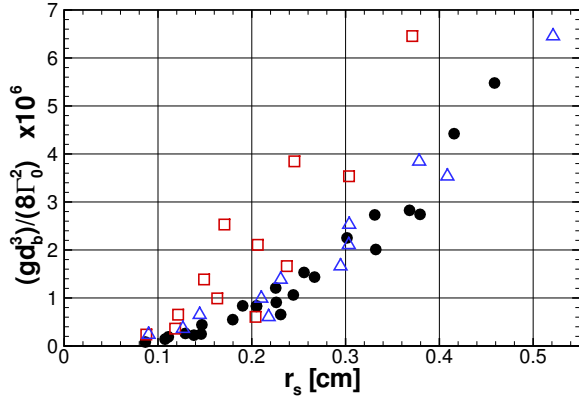radius, particularly as the ratio of bubble size to vortex strength is increased.

Figure 11: Comparison of the non-dimensional settling location with the experimental results of Sridhar and Katz (1999). The parameter $gd_b^3/8\Gamma^2$ is the non-dimensional ratio of the buoyancy force and the hydrodynamic pressure gradient experienced by the bubble. (●) Experimental data, □ two-way coupling (neglecting volumetric effects), △ volumetric coupling.

Importantly, significant vortex distortion is predicted by the numerical model for certain bubbles with parameters similar to those observed in the experiments. In the absence of the bubbles, the vortex core is stable as shown in figure 12a. In the presence of some entrained bubbles, the vortex core deforms, altering the vorticity distribution as shown in figure 12b. The contours of vorticity in figure 12b are shown approximately 1 second after bubble entrainment. The core has been fragmented into several regions of higher vorticity. Figure 12c shows how the average radial vorticity distribution is changed because of the presence of the bubbles. In the undistrubed state, the vorticity distribution is very close to that of the Gaussian vortex from the first test case. The volumetric displacement of the fluid due to bubble motion results in a decrease of inner core vorticity, while a band of high vorticity has been created just outside of the bubble settling radius. As a quantitative measure, we calculate the change in the decay rate of angular momentum, illustrated in figure 12d for each case with and without bubbles. The instantaneous vortex angular momentum is calculated by summing the momentum of all control volumes in the core

$$L_{vx} = \sum_{core\ cv's} \rho_f U_\theta r_{cv} V_{cv} \qquad (28)$$

Where r_{cv} is the distance from the vortex centroid to the cv center and V_{cv} is the cv volume. The decay rate is

then just the time derivative of the angular momentum.

$$\text{Decay rate} = \epsilon = \frac{d(L_{vx})}{dt} \qquad (29)$$

In *all* cases, we observe an increase of the decay rate from ϵ to $\hat{\epsilon}$ when considering volumetric coupling, although the relative amount of this increase varies significantly. To normalize the amount across all cases, we introduce the relative change in decay rate,

$$\text{Relative change in decay rate (\%)} = E = \frac{\overline{\hat{\epsilon} - \epsilon}}{\epsilon} \times 100 \qquad (30)$$

The overbar denotes the average decay rate measured between $X = 5.2h_{jet}$ to $X = 5.8h_{jet}$. Values of E range 1% for $500\mu m$ bubbles entrained in a vortex with $\Gamma_0 = 0.0254m^2s^{-1}$, to almost 150% for, $1,100\mu m$ bubbles entrained in a vortex with $\Gamma_0 = 0.0159m^2s^{-1}$. These characteristics of vortex distortion were found to be predominantly an effect of variations in the void fraction as the bubbles travel to their settling location. This was confirmed by computing the bubble trajectories without considering the void fraction variations. With two-way coupling and neglecting volumetric displacement effects (i.e. Θ_f set equal to 1), vortex distortion was not obtained for any of the cases studied. This confirms the effectiveness of the present numerical model in properly predicted bubble-vortex interactions.

A correlation for decay of angular momentum
The increase in vortex decay rate varies significantly depending on bubble size and vortex strength. Increasing bubble size (or decreasing the fluid volume fraction) seems to have an effect, as does decreasing the vortex strength. Here, we develop an analysis to understand how this increase in the vortex decay rate scales with the magnitude of the highly local, bubble-fluid interactions. We start by calculating the net reaction force acting on the fluid due to the presence of the bubbles with volumetric coupling. A similar analysis was conducted by Sridhar and Katz (1999); Druzhinin and Elghobashi (1998). We will derive an expression here applicable to the current Eulerian-Lagrangian framework, and use it to calculate the net reaction from the entrained bubbles at their settling location in a Gaussian vortex. We can write the single phase, undisturbed momentum equation as:

$$\mathbf{C} = \mathbf{P} + \mathbf{V} + \mathbf{B}, \qquad (31)$$

where $\mathbf{C}$ denotes the convective fluid acceleration term, $\mathbf{P}$ denotes the pressure term, $\mathbf{V}$ the viscous term, and $\mathbf{B}$ the gravitational body force term. Similarly for multiphase flow, the volume averaged momentum equation (equation 14) can be expressed as

$$\hat{\mathbf{C}} = \hat{\mathbf{P}} + \hat{\mathbf{V}} + \hat{\mathbf{B}} + \mathbf{f} \qquad (32)$$
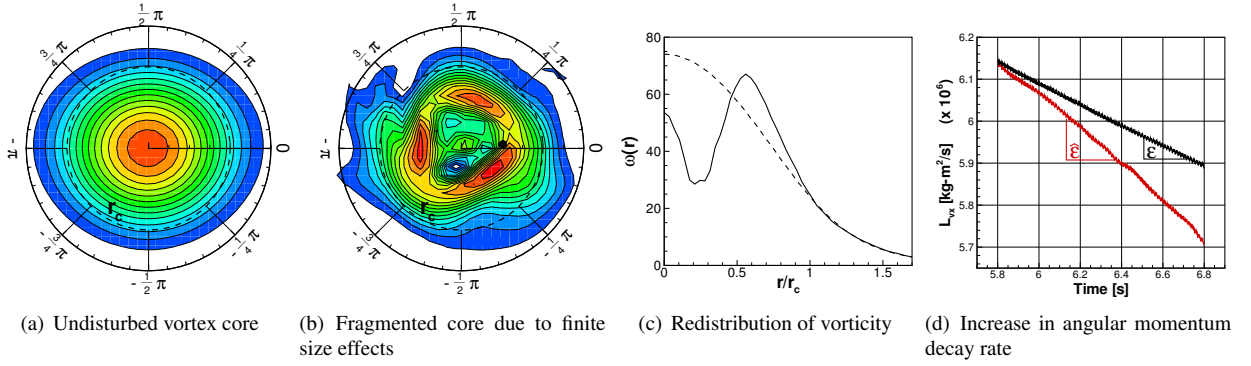
(a) Undisturbed vortex core | (b) Fragmented core due to finite size effects | (c) Redistribution of vorticity | (d) Increase in angular momentum decay rate

Figure 12: Characteristic changes observed in distorted vortex cores due to the presence of bubbles with finite size: (a) Undisturbed vorticity contours, (b) vorticity contours and average bubble location (black dot) with finite size effects, (c) radial re-distribution of vorticity (- - -) without void fraction variations, (—) with void fraction variations, (d) increase in decay rate of angular momentum from ϵ without bubbles to $\hat{\epsilon}$ with bubbles and accounting for void fraction variations.

Here, $\hat{\mathbf{C}}$, $\hat{\mathbf{P}}$, $\hat{\mathbf{V}}$, and $\hat{\mathbf{B}}$ are the same contributions to the fluid momentum, but are representative of the disturbed flow field containing the eight finite size bubbles. If all terms are moved to the right hand side, and the single phase terms are subtracted from the disturbed flow terms, we can write an expression for the reaction force per volume imposed on the fluid by the presence of the dispersed phase:

$$\Delta\mathbf{R} = \left(\mathbf{C} - \hat{\mathbf{C}}\right) + \left(\hat{\mathbf{P}} - \mathbf{P}\right) + \left(\hat{\mathbf{V}} - \mathbf{V}\right) + \left(\hat{\mathbf{B}} - \mathbf{B}\right) + \mathbf{f}$$
(33)

In order to simplify this and arrive at an expression applicable to the present case, we make the following assumptions. First, the undisturbed flow is steady over the timescale of bubble to fluid momentum transfer. Second, the bubbles are not accelerating. Once they reach their settling location, they translate rectilinearly with the vortex core. This also implies that the lift, drag, added mass, pressure, and gravity forces are in balance. Finally, we assume the vortex core is well represented by the axisymmetric, Gaussian profile. This can be seen in figure 12c. The advantage to this assumption is that we now have good estimates for velocity, vorticity, and dynamic pressure gradient in the undisturbed vortex core. The individual terms in equation 33 can then be simplified as follows:

$$\mathbf{C} \quad -\hat{\mathbf{C}} = \rho_f \frac{D\mathbf{u}}{Dt} - \frac{D\left(\Theta_f\rho_f\mathbf{u}\right)}{Dt} \approx \rho_f\Theta_b\frac{u_\theta^2}{r}$$

$$\hat{\mathbf{P}} \quad -\mathbf{P} = \nabla P - \nabla P = 0 \qquad (34)$$

$$\hat{\mathbf{V}} \quad -\mathbf{V} \approx \mu\nabla\left(\Theta_f\nabla\mathbf{u}\right) - \mu\nabla^2\mathbf{u} \approx \text{small if } \mu << 1$$

$$\hat{\mathbf{B}} \quad -\mathbf{B} = \Theta_f\rho_f\mathbf{g} - \rho_f\mathbf{g} = -\Theta_b\rho_f\mathbf{g}$$

$$\mathbf{f} \quad = -\left(\mathbf{F}_D + \mathbf{F}_L + \mathbf{F}_{AM} + \mathbf{F}_P\right) = \mathbf{F}_G = \Theta_b\rho_b\mathbf{g}$$

The change in fluid body force can be combined with the interphase reaction term, $\mathbf{f}$, to form a net buoyancy force experienced by the fluid. Note that the interphase reaction term will be small when the bubbles are not accelerating, explaining why the point particle two-way coupling approach causes almost no vortex distortion. The only other significant term which arises in this simplification is due to changes to the dynamic pressure gradient, $\rho_f u_\theta^2/r$. If all terms are combined, and we multiply through by the fluid volume, then the total reaction force to the fluid because of n bubbles having volume V_b becomes:

$$\Delta\mathbf{R} = nV_b\left(\frac{\rho_f u_\theta^2}{r_s} + \mathbf{g}(\rho_b - \rho_f)\right) \qquad (35)$$

This is in agreement with the general expression obtained by Druzhinin & Elghobashi for their two-fluid model, and used by and Sridhar & Katz in their discussion of bubble induced vortex distortion. In order to find the magnitude of the total reaction to the fluid, we must decompose the reaction into components. In a cylindrical coordinate system located at the vortex center we have.

$$R_r = nV_b\left[\frac{\rho_f u_\theta^2}{r} - \mathbf{g}\left(\rho_b - \rho_f\right)\sin(\theta_s)\right] \quad (36)$$

$$R_\theta = nV_b\mathbf{g}\left(\rho_b - \rho_f\right)\cos(\theta_s) \qquad (37)$$

In the present clockwise vortices, the magnitude of this reaction will be directed up and to the left from the settling location in first quadrant. The magnitude and direction of the net reaction measured from the horizontal

($\theta = 0$) will be

$$R_{net} = \sqrt{R_r^2 + R_\theta^2} \qquad (38)$$

$$\theta_R = \theta_s + \frac{\pi}{2} + \arctan\left(\frac{R_r}{R_\theta}\right) \qquad (39)$$

The net reaction, R_{net}, represents a local input to the fluid. Intuitively, the local force which drives the rotation of the vortex should also dictate the magnitude of the observed effects. We therefore choose to normalize, R_{net}, by the local vortex force, F_{vx}^{local}. The idea of the vortex force was originally put forth by Prandtl (1918) and is frequently used when studying vortex dynamics (see Saffman (1995)). It can be thought of as the force required to maintain steady rotation of a vortex. It is defined for a closed region as

$$\mathbf{F}_{vx} = \int \mathbf{u} \times \omega \, dV \qquad (40)$$

If we insert the expressions for the Gaussian vortex velocity and vorticity fields given in the first test case, we can obtain an expression for the total vortex force required to drive the Gaussian vortex having initial strength Γ_0 and core radius, r_c.

$$F_{vx} = \frac{\Delta z \Gamma_0^2 \eta_1}{2\pi r_c^2} \int_0^{r_c} \left[e^{-\eta_1(r/r_c)^2} - e^{-2\eta_1(r/r_c)^2} \right] dr \qquad (41)$$

Here, the cross product in the integral has been simplified because the velocity, u_θ is orthogonal to the vorticity, ω_z at all points in the undisturbed, 2D vortex core. Using this expression, a more helpful quantity is the vortex force required to maintain rotation of a small band centered at the bubble settling radius, illustrated schematically in figure 13. By changing the integration limits in equation 41 to represent a band of width δ, centered at the bubble settling radius, r_s, we obtain

$$F_{vx}^{local} = \frac{\Delta z \sqrt{2\eta_1} \Gamma_0^2}{8\sqrt{\pi} r_c} [\mathcal{A}]_{r_s - \frac{\delta}{2}}^{r_s + \frac{\delta}{2}} \cdot \frac{r_c}{\delta}, \qquad (42)$$

$$\mathcal{A} = \sqrt{2} \, \mathrm{erf}\left(\sqrt{\eta_1}\frac{r}{r_c}\right) - \mathrm{erfc}\left(\sqrt{2\eta_1}\frac{r}{r_c}\right)$$

Note, that the integration has been post-mulitplied by the scaling quantity r_c/δ. This is to account for the effect that choice of bandwidth has on the magnitude of the integral. By rescaling in this way, the values of vortex force become independent of the choice of δ so long as $\delta << r_c$.

Using the bubble settling coordinates predicted with volumetric coupling, the net reaction, R_{net} and local vortex force, F_{vx}^{local}, are calculated for each of the 12 cases with volumetric coupling. The net reaction is then normalized by the local vortex force to compute a relative reaction force, $R_{rel} = R_{net}/F_{vx}^{local}$. This relative
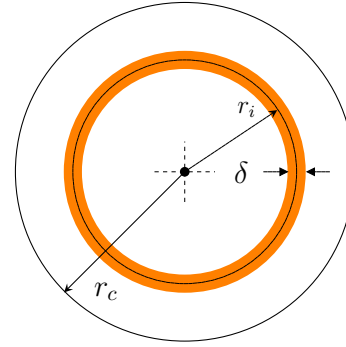

Figure 13: Schematic of differential band used to integrate the local vortex force.

reaction can be thought of as a potential for vortex distortion, or momentum redistribution. The relative decrease in vortex decay rate, E, is plotted against R_{rel} in figure 14. The figure shows that the relative reaction force is capable of both collapsing the values of E and also producing a highly linear trend across the datapoints. There are two important implications of this result. First, we see that the local vortex force is a valuable scaling parameter for normalizing the interphase reaction force. Determining a local measure of the vortex force in this case was straightforward because of the good match with the Gaussian flow field. For an arbitrary flowfield such as homogenous turbulence, a more general approach would need to be taken. Second, we have obtained a correlation between a large scale vortex property, E, and a property associated with the local bubble-scale interactions, R_{rel}. This could be coupled with a model for the settling coordinates such as the one developed in the stationary vortex section, to arrive at a lower order model for bubble induced vortex attenuation based solely on the parameters Γ_0, r_c, and d_b.

Conclusions

The present work focussed on using a discrete element model (DEM) for simulation of bubble or particle interactions with vortical flows. The volumetric displacement of the fluid by the subgrid scale dispersed phase, along with point particle momentum exchange were used for realistic coupling of the dispersed phase to the fluid. The numerical implementation of the DEM model was first evaluated for cases involving vortical flows and dense loadings where the volume displacement effects are considerably large: (i) a rising bubble plume, and (ii) a falling blob of particles. The results show good agreements with published data. Next, the effectiveness and importance of volumetric coupling even under dilute loading was evaluated by simulate interactions of
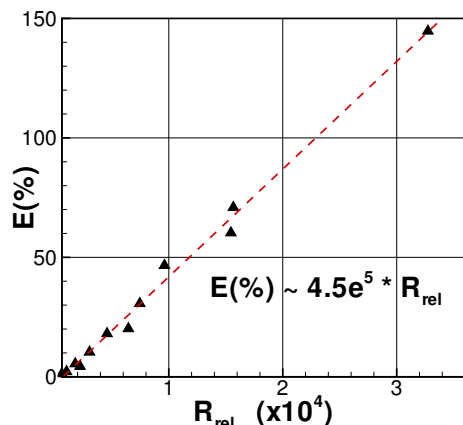
Figure 14: Linear relationship between E and R_{rel} for each of the 12 cases simulated with volumetric coupling.

few small bubbles with a traveling vortex tube. This corresponds to a two-dimensional approximation of the experiments on traveling vortex rings by Sridhar and Katz (1999). It was shown that accounting for the *volumetric displacement* of fluid by the dispersed phase is critical in predicting the correct bubble settling location as well as capturing the experimentally observed distortion. In our simulations, we notice a secondary effect, which is an increase in the angular momentum decay rate due to the finite size of bubbles. To better understand the variation in the magnitude of these changes, a method for determining a relative reaction force was developed using the idea of a local vortex force. This potential can be thought of as the relative ability of the bubbles to cause change to the vortex flow structure. For the Gaussian type vortices studied in this work, it is based entirely on the bubble size, vortex size, the vortex strength. The results show a linear correlation between this distortion potential and the observed relative increases in vortex decay rate. This important relationship shows how local bubble scale interactions can be related to vortex scale strength attenuations. This study has important consequences in understanding bubble interactions with coherent vortical structures in turbulent flows.

Acknowledgements

References

SV Apte, K. Mahesh, P. Moin, and JC Oefelein. Large-eddy simulation of swirling particle-laden flows in a coaxial-jet combustor. *International Journal of Multiphase Flow*, 29(8):1311–1331, 2003.

SV Apte, K. Mahesh, and T. Lundgren. Accounting for finite-size effects in simulations of disperse particle-laden flows. *International Journal of Multiphase Flow*, 2007.

S. Becker, A. Sokolichin, and G. Eigenberger. Gas-liquid flow in bubble columns and loop reactors. II: Comparison of detailed experiments and flow simulations. *Chemical engineering science*, 49(24 B):5747–5762, 1994.

E. Climent, M. Simonnet, and J. Magnaudet. Preferential accumulation of bubbles in Couette-Taylor flow patterns. *Physics of Fluids*, 19:083301, 2007.

D. Darmana, NG Deen, and JAM Kuipers. Detailed modeling of hydrodynamics, mass transfer and chemical reactions in a bubble column using a discrete bubble model. *Chemical Engineering Science*, 60(12):3383–3404, 2005.

D. Darmana, NG Deen, and JAM Kuipers. Parallelization of an Euler–Lagrange model using mixed domain decomposition and a mirror domain technique: Application to dispersed gas–liquid two-phase flow. *Journal of Computational Physics*, 220(1):216–248, 2006.

NG Deen, T. Solberg, and BH Hjertager. Numerical Simulation of the Gas-Liquid Flow in a Square Cross-sectioned Bubble Column. In *14th Int. Congress of Chemical and Process Engineering. Praha-Czech Republic*. Citeseer, 2000.

E. Delnoij, FA Lammers, JAM Kuipers, and WPM Van Swaaij. Dynamic simulation of dispersed gas-liquid two-phase flow using a discrete bubble model. *Chemical engineering science*, 52(9):1429–1458, 1997.

OA Druzhinin and S. Elghobashi. Direct numerical simulations of bubble-laden turbulent flows using the two-fluid formulation. *Physics of Fluids*, 10:685, 1998.

A. Ferrante and S. Elghobashi. On the physical mechanisms of two-way coupling in particle-laden isotropic turbulence. *Physics of Fluids*, 15:315, 2003.

A. Ferrante and S.E. Elghobashi. On the effects of microbubbles on Taylor–Green vortex flow. *Journal of Fluid Mechanics*, 572:145–177, 2007.

D. Gidaspow. *Multiphase flow and fluidization: continuum and kinetic theory descriptions*. Academic Pr, 1994.

G. Hu and I. Celik. Eulerian–Lagrangian based large-eddy simulation of a partially aerated flat bubble column. *Chemical Engineering Science*, 63(1):253–271, 2008.

R. Jackson. Locally averaged equations of motion for a mixture of identical spherical particles and a Newtonian fluid. *Chemical Engineering Science*, 52(15):2457–2469, 1997.

D.D. Joseph, T.S. Lundgren, R. Jackson, and DA Saville. Ensemble averaged and mixture theory equations for incompressible fluid-particle suspensions. *Int. J. Multiphase Flow*, 16(1):35–42, 1990.

TS Lundgren. Slow flow through stationary random beds and suspensions of spheres. *Journal of Fluid Mechanics*, 51(02):273–299, 1972.

I.M. Mazzitelli, D. Lohse, and F. Toschi. The effect of microbubbles on developed turbulence. *Physics of Fluids*, 15:L5, 2002.

C. Mitts, D. Talley, and D. Poulikakos. A fundamental study of supercritical droplet deformation and breakup through a miscible fluid analog. In *AIAA, ASME, SAE, and ASEE, Joint Propulsion Conference and Exhibit, 32 nd, Lake Buena Vista, FL*, 1996.

P. Moin and SV Apte. Large-Eddy Simulation of Realistic Gas Turbine-Combustors. *AIAA journal*, 44(4): 698–708, 2006.

GF Oweis, IE van der Hout, C. Iyer, G. Tryggvason, and SL Ceccio. Capture and inception of bubbles near line vortices. *Physics of Fluids*, 17:022105, 2005.

A. Prosperetti and DZ Zhang. Finite-particle-size effects in disperse two-phase flows. *Theoretical and Computational Fluid Dynamics*, 7(6):429–440, 1995.

PG Saffman. The lift on a small sphere in a slow shear flow. *Journal of Fluid Mechanics*, 22(02):385–400.

PG Saffman. *Vortex dynamics*. Cambridge University Press, 1995.

L. Schiller and A. Naumann. A drag coefficient correlation. *Vdi Zeitung*, 77:318–320, 1935.

E. Shams. *Numerical simulation of cavitating bubble-laden turbulent flows, Ph.D. Thesis, Oregon State University*. Oregon State University, 2010.

A. Sokolichin and G. Eigenberger. Applicability of the standard k–ε turbulence model to the dynamic simulation of bubble columns: Part I. Detailed numerical simulations. *Chemical Engineering Science*, 54(13-14): 2273–2284, 1999.

G. Sridhar and J. Katz. Drag and lift forces on microscopic bubbles entrained by a vortex. *Physics of Fluids*, 7:389, 1995.

G. Sridhar and J. Katz. Effect of entrained bubbles on the structure of vortex rings. *Journal of Fluid Mechanics*, 397:171–202, 1999.

MA van der Hoef, M. van Sint Annaland, NG Deen, and JAM Kuipers. Numerical Simulation of Dense Gas-Solid Fluidized Beds: A Multiscale Modeling Strategy. *ANNUAL REVIEW OF FLUID MECHANICS*, 40:47, 2008.

E.A. Van Nierop, S. Luther, J.J. Bluemink, J. Magnaudet, A. Prosperetti, and D. Lohse. Drag and lift forces on bubbles in a rotating flow. *Journal of Fluid Mechanics*, 571:439–454, 2007.

JH Walther and P. Koumoutsakos. Three-dimensional vortex methods for particle-laden flows with two-way coupling. *Journal of Computational Physics*, 167(1): 39–71, 2001.

DZ Zhang and A. Prosperetti. Momentum and energy equations for disperse two-phase flows and their closure for dilute suspensions. *International Journal of Multiphase Flow*, 23(3):425–453, 1997.